In situ-formed nitrogen-doped carbon/silicon-based materials as negative electrodes for lithium-ion batteries

Monje, Ivonne E.

2021-11-15

Monje , I E , Sanchez-Ramirez , N , Santagneli , S H , Camargo , P H , Belanger , D , Schougaard , S B & Torresi , R M 2021 , ' In situ-formed nitrogen-doped carbon/silicon-based materials as negative electrodes for lithium-ion batteries ' , Journal of Electroanalytical Chemistry , vol. 901 , 115732 . https://doi.org/10.1016/j.jelechem.2021.115732

http://hdl.handle.net/10138/354259
https://doi.org/10.1016/j.jelechem.2021.115732

In situ-formed nitrogen-doped carbon/silicon-based materials as negative electrodes for lithium-ion batteries

Ivonne E. Monje[*,a,e], Nedher Sanchez-Ramirez[a,b], Silvia H. Santagneli[c], Pedro H. Camargo[a,d], Daniel Bélanger[e], Steen B. Schougaard[e] and Roberto M. Torresi[*,a]

[a]*Departamento de Química Fundamental, Instituto de Química – Universidade de São Paulo, Av. Prof. Lineu Prestes 748, 05500-000, São Paulo, Brazil*

[b]*Departamento de ciencias, Universidad de Ingenieria y Tecnologia – UTEC, Barranco, Peru*

[c]*Instituto de Química. UNESP, Rue Francisco Degni, 55, 14800-060 - Araraquara, São Paulo. Brazil*

[d]*Department of Chemistry, University of Helsinki, A.I. Virtasen Aukio 1, 00014 Helsinki, Finland*

[e]*NanoQAM and Département de Chimie Université du Québec à Montréal, Case Postale 8888 Succursale Centre-Ville, Montréal, Québec, H3C 3P8, Canada*

Abstract

The development of negative electrode materials with better performance than those currently used in Li-ion technology has been a major focus of recent battery research. Here, we report the synthesis and electrochemical evaluation of *in situ*-formed nitrogen-doped carbon/SiOC. The materials were synthesized by a sol-gel process using 3-(aminopropyl)triethoxysilane (APTES), sodium citrate and glycerol. The electrochemical performance of pyrolyzed materials was studied using poly(acrylic acid) binder and commercial organic electrolyte. Our reported approach enables changes in both the amount of nitrogen and the morphology as a function of the molar ratio of APTES:citrate and reaction time. Spherical-shaped NC/SiOC composite electrodes deliver a delithiation capacity of 622 mAh/g at 0.1 A/g and an initial coulombic efficiency of ~63%, while in the large bulk material, respective values of 367 mAh/g and ~55% were obtained. After 1000 charge/discharge cycles at 1.6 A/g, the latter material exhibits 98% of the initial capacity once it returned to lower current cycling. Overall, our results indicate that NC/SiOC materials are quite promising for electrochemical applications since both their large capacity and stability demonstrate superior performance compared to traditional graphite. Moreover, our synthesis is simple and, more importantly, environmentally friendly chemicals, such as sodium citrate and glycerol, are used.

Keywords: Lithium-ion batteries; silicon oxide; silicon oxycarbide; nitrogen-doped carbon; negative electrode.

* Corresponding authors. Tel: 011-30912165. E-mail: rtorresi@iq.usp.br (Roberto M. Torresi) and ivonneeliana@gmail.com (Ivonne E. Monje).

1. Introduction

The current state-of-the-art negative electrode technology of lithium-ion batteries (LIBs) is carbon-based (i.e., synthetic graphite and natural graphite) and represents more than 95% of the negative electrode market[1]. Market demand is strongly acting on LIB manufacturers to increase the specific energy and reduce the cost of their products[2]. Therefore, identifying new negative electrode materials with better performance than those currently used in Li-ion technology has been a major focus of recent battery research.

Silicon, having a theoretical specific capacity of ~4200 mAh/g ($Li_{4.4}$ Si), much higher than that of graphite (~372 mAh/g)[3,4], has been regarded as one of the most promising materials for the next generation of LIBs. However, major drawbacks of silicon are related to its volume expansion upon Li alloying during charging and the continued formation of a fresh solid electrolyte interphase (SEI) due to the cracking of active material grains exposing a new negative electrode surface to the electrolyte[5]. To date, tremendous efforts have been made to overcome these problems. Although extensive coating, binder[6], electrolyte[7], additive, and nanomaterial designs (i.e., silicon nanoparticles) have been studied, and despite some improvements, the costs and production methods are still not satisfactory and/or comparable to those of carbon-based materials[5],[8]. Therefore, finding alternative approaches to produce low-cost negative electrodes with high performance is needed to ensure the future massive use of LIBs in urban transportation or as an energy storage system for renewable energies.

Silicon oxycarbides ($SiO_{(4-x)}C_x$, x=1-4, i.e., SiO_4, SiO_3C, SiO_2C_2, $SiOC_3$, and SiC_4) have attracted significant attention as negative electrode materials due to their different possible active sites for lithium insertion/extraction and lower volumetric changes than silicon[9–13]. As a carbon-containing silicate ceramic, they consist of an amorphous

SiOC glass phase and free carbon phase. In their structures, a silicon central atom is bonded to oxygen and/or carbon atoms, forming a tetrahedral unit, in which carbon atoms bonded to silicon have sp^3-hybridization, while those in the free carbon phase form sp^2-hybridization [10].

The origin of lithium storage and the nature of electrochemically active sites are still controversial. It has been proposed that the active sites are *i)* a mixed bond configuration of tetrahedral coordinated silicon[4]; *ii)* the free carbon phase, interstitial and/or edges of the graphene-like structure; and *iii)* micropores, since lithium ions can be absorbed into the formed free carbon phase of turbostratic carbon[10,14–16]. Despite these potential outstanding features given by the multiple possible sites for Li^+ insertion, major concerns include both the low electrical conductivity and low initial Coulombic efficiency. Among the strategies used to solve these drawbacks to improve the electrochemical performance are tailoring the amount of free carbon by varying the substituents directly attached to silicon atoms[10,17] and developing SiOC/carbonaceous hybrid materials[18]. For instance, SiOC with exfoliated graphite[19], carbon nanotubes[20], carbon nanofibers[21], and graphene[9,22] has been employed for negative electrodes, and interesting results in terms of stability and delithiation capacities have been reported.

Similarly, other approaches based on introducing nitrogen into carbon structures mixed with silicon-based materials have been shown to enhance the energy storage ability and Li^+ transport by creating defects and improving the electronic conductivity[8,23–28]. For instance, N-doped carbon/SiO_2[26], N-doped carbon coatings/SiO[25], N-doped carbon/Si[27], and N-doped graphitic layers/Si nanowires[28] have been reported. Despite the interesting features of nitrogen-doped carbon, N-doped carbon/SiOC materials have attracted little attention. Free-standing N-doped carbon nanofibers/SiOC were synthesized through a multistep process based on a mixture of ball-milled HF-etched SiOC and PAN/DMF followed by electrospinning and pyrolysis. The synthesized material delivered a discharge capacity of 595 mAh/g at 0.2 mA/g, while in the undoped material, 400 mAh/g at 0.2 mA/g was obtained. This superior performance was attributed to the fact that nitrogen atoms present in the carbon fiber induce more defects and create more lithium storage sites[29].

This paper describes the development of a facile strategy for the *in situ* preparation of N-doped carbon with silicon oxycarbide by employing 3-(aminopropyl)triethoxysilane (APTES) and low-cost and environmentally friendly sodium citrate and glycerol. More specifically, our approach is based on the dual ability of APTES to act as a siloxane precursor and as an N source for the formation of N-doped graphene-like structures when reacting with sodium citrate[30]. No additional functionalization steps or external nitrogen-carbon sources were required. APTES is extensively employed as coupling agent for attaching organic moieties to inorganic oxides[31,32] and it is quite relevant in the immobilization of biomolecules[33]. However, here we propose its use as SiOC precursor, which has been scarcely reported. In addition, APTES can be considered an interesting choice for commercial systems due to the inherently lower cost relative to others SiOC precursors such as 1,3,5,7-Tetravinyl-1,3,5,7-tetramethylcyclotetrasiloxane (TTC)[4,34], phenyltriethoxysilane (PhTES)[35], Vinyltriethoxysilane (VTES)[35,36] and Methyltriethoxysilane MTES[35,37], as is reflected in the commercial price (USD/2Kg) [38]): APTES (100) <MTES (118) <VTES(140) <PhTES (146) <TTC (488). The synthesis method explored allows us to obtain sphere-like silicon oxycarbide particles without using any catalyst or templates commonly used for the formation of spherical SiOC and to vary the amount of N in the carbon as a function of both the APTES:citrate molar ratio and reaction time. To examine the electrochemical performance of the materials synthesized as negative electrodes for LIBs, composite electrodes were prepared using poly(acrylic)acid (PAA) as the binder and commercial organic electrolyte.

2. Materials and methods

2.1 N-doped C/SiOC synthesis and composite electrode preparation

N-doped carbon/silicon oxycarbide (NC/SiOC) active materials were synthesized by procedures adapted for the synthesis of silicon nanoparticles and nitrogen-doped graphene quantum dots for immunofluorescence applications or bioimaging[30,39,40].

The synthesis method is described in Scheme S1. In a typical synthesis of the NC/SiOC-81-1h sample (APTES:citrate molar ratio of 8:1), nitrogen gas was bubbled in 32 ml of glycerol (l,2,3-propanetriol, 99% ACS) at room temperature for 1 h with magnetic stirring. Then, in a continuous nitrogen atmosphere, 2.16 mmol of sodium citrate tribasic dihydrate (99% ACS) was loaded into a two-neck round-bottom flask.

Subsequently, 17.30 mmol of APTES (3-aminopropyltriethoxysilane, purity>98% v/v, Sigma-Aldrich) was slowly added into the solution. The preceramic polymers were cross-linked at 100 °C for 1 h and then cooled to room temperature. After 24 h, the reaction mixture was heated to 180 °C for 1 h under continuous nitrogen flux and magnetic stirring. Glycerol was removed, and the reaction product was cleaned by dialysis with 14 kDa tubing (Sigma-Aldrich). After drying in vacuum at room temperature, the preceramic powder was pyrolyzed in argon at 1000 °C for 1 h. The same procedure was followed for the NC/SiOC-88-3h sample, in which the molar ratio of APTES:citrate was 8.3:8:3 mmol, and 3 h at 180 °C was chosen as the temperature and reaction time, respectively.

The NC/SiOC powder (120-150 mg) obtained after pyrolysis was finely crushed in a mortar. The electrodes were prepared as follows: the active material (108 mg), the poly(acrylic acid) (PAA, Sigma-Aldrich) (36 mg) binder and the acetylene black carbon (Alfa Aesar) (36 mg) conducting additive matrix were mixed in a mortar and pestle and transferred to a 5 mL beaker that contained 0.7 mL of anhydrous ethanol. The weight ratio was kept constant in all experiments at 60% NC/SiOC active material, 20% acetylene black, and 20% binder. Then, the electrode slurries were thoroughly mixed using a laboratory stirrer (600 rpm) for at least 8 h, cast on Cu foil, and dried in vacuum at 80 °C for 3 h. Subsequently, the electrode disks were punched out into circular disk with a mass loading of ca. 0.6-0.8 mg (~0.3-0.4 mg/cm^{-2}), and the electrode thickness was 23-24 μm. All electrodes were kept in an argon-filled glovebox and not exposed to air prior to assembling the test cells.

2.2 Material characterization

Microstructural analyses of the powders were carried out by using a JEOL Model 2100F FEG-TEM microscope operating at an accelerating voltage of 200 kV. For bright field imaging and EDS X-ray spectra collection, an Oxford model Xplore system was used. The SEM images were obtained with a JEOL JSM-7600F system equipped with a field emission gun (FEG) and a resolution of 1.0 nm at 15 kV.

Solid-state NMR experiments were performed on the ^{29}Si nuclei with a Bruker Avance III HD 400WB-equipped spectrometer (9.4 T) using a 4 mm double resonance probe. The experiments were conducted at a spinning speed of 10 kHz. The ^{29}Si{^{1}H} cross-polarization (CP) were recorded using a contact time of 4.5 ms, a relaxation delay of 2

s, and a two-pulse phase-modulation (TPPM) proton decoupling was used during data acquisition. The chemical shifts are reported relative to the TMS reference standard.

Raman spectra were obtained with a Renishaw inVia dispersive confocal Raman microscope using 532 nm laser excitation lines. Spectra were distorted by underlying fluorescence, and baseline subtraction was employed. A third-order polynomial function was used for background correction, the spectra were smoothed, and the Voigt deconvolution function was used (Fig. S2 in the supplementary information).

The powdered samples were also characterized by X-ray powder diffraction (XRD) using a Bruker D8 Advance diffractometer. Diffractograms were obtained using Cu Kα radiation at 40 kV and 40 mA in the range of 20–80° (2ϴ) with a step size of 0.05° and a scan rate of 1°/min. Thermogravimetric analysis was conducted in synthetic air with a TGA Instrument Q500 system. Samples were heated to 950 °C with a heating rate of 10 °C/min and an air flux rate of 90 ml/min. The elemental analysis was determined by the inert gas fusion method using a Leco RH-404 hydrogen analyzer, TC-436 oxygen-nitrogen analyzer and Leco CS-200 carbon-sulfur analyzer using combustion infrared detection for carbon quantification. The amount of silicon was calculated from the difference. Brunauer–Emmett–Teller (BET) surface areas were measured at 77 K with a Micrometrics Tristar II Plus instrument, and the samples were degassed at 120 °C overnight under vacuum. Surface chemistry analysis was performed on the samples using a commercial UNI-SPECS UHV spectrometer with Mg Kα radiation (hν = 1254.6 eV) and a chamber pressure maintained at $<5x10^{-7}$ Pa. The binding energy scale was corrected by using the C 1s main peak at 284.4 eV. After using the Shirley method for background subtraction, the raw spectra were fitted using Voight functions, Gaussian (70%) and Lorentzian (30%) functions.

Electrochemical measurements were performed with a two-electrode CR2032 coin cell configuration using a VMP3 BioLogic potentiostat. The coin cells were assembled using NC/SiOC composite electrodes as working electrodes, lithium metal foil (Alfa Aesar purity>99.9%) as the counter electrode, Celgard 2320 as the separator and commercial 1 mol L^{-1} $LiPF_6$ in mixed solvents of ethylene carbonate (EC)/diethyl carbonate (DEC) (50:50 v/v) (Sigma Aldrich) as the electrolyte. The cells were cycled, discharged (lithiated), and charged (delithiated) in galvanostatic mode at room temperature between 0.05 and 2.5 V cutoff potentials vs. Li/Li^+. Electrochemical

measurements of half-cells were all normalized based on the mass of the NC/SiOC active material.

The rate capabilities of the composite electrodes were evaluated at various current densities ranging from 0.1 to 2.4 A/g. Coulombic efficiencies were also calculated with $((C^{dealloy})/(C^{alloy}))$ x 100, where C^{alloy} and $C^{dealloy}$ are the capacity of the negative electrode for lithiation and delithiation, respectively.

3. Results and discussion

3.1 Materials synthesis

Fig. 1 presents the surface morphology of both NC/SiOC materials obtained after pyrolysis. The SEM micrographs (Fig. 1A and 1B) show that both samples seem to form irregular large-sized (>0.01 mm) particles. However, a higher magnification of the surface (Fig. 1C-F) indicates that sample 81-1h consists of interconnected spheres that are approximately 500 nm in size. In contrast, for sample 88-3h, the particle surface is almost flat and almost free of smaller particle features. The selected area electron diffraction (SAED) pattern of the particles shown in Fig. 1E and 1F (bottom inset) shows the absence of crystalline areas, in agreement with the XRD patterns shown in Fig. 2A.

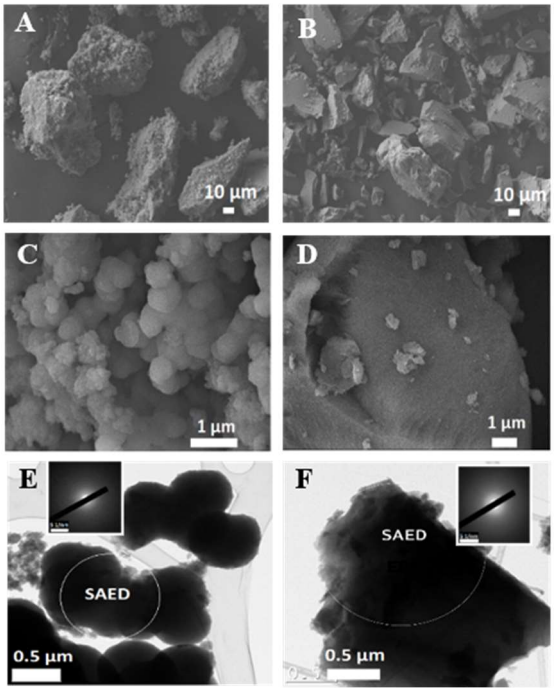

Figure 1. SEM images (A-D), TEM images (E and F) and SAED patterns (insets) of NC-SiOC 81-1h (A, C and E) and NC-SiOC 88-3h (B, D and F).

The diffractograms show a broad and asymmetrical peak centered at approximately 22°-25°, which indicates both the amorphous features of SiOC-SiO_2 ceramics, typically centered at 2ϴ= 22°[17,41,42], and the disordered turbostratic carbon phase with a peak at 2ϴ=25.4° and a shoulder at approximately 43°[43,44]. In addition, a slight shoulder at approximately 2ϴ=30° may suggest the presence of amorphous nanosized silicon[45]. The Raman spectra (Fig. 2B) further confirm the presence of the disordered graphitic forms of carbon, with a D_1 band (so-called disorder-induced) at approximately 1335 cm^{-1} and a G band (1591 cm^{-1}) related to sp^2 hybridized C atoms[46,47]. Additionally, the 2D (an overtone of the D band) and D + G bands at ~2680 and ~2945 cm^{-1} can be observed, respectively.

For further characterization, after background and smoothing corrections, the spectra in the region between 1300 and 1600 cm^{-1} were curve-fitted into four bands (Fig. S2). In addition to the conventional D_1 and G bands, D_3~1500 and D_4~1220 cm^{-1} are shown[48,49]. Although the number of disordered bands that are separated using curve fitting and their attribution are still controversial, the intensity and features of additional D bands provide information about disorder in carbon materials. Peak D_4 was attributed to the presence of sp^2–sp^3 C–C and C=C bonds, while the important contribution of D_3, related to the fraction of amorphous carbon, confirms the high disorder degree of the samples[50]. The I_{D1}/I_G ratios are calculated to be 1.01 and 1.17 for the 88-3h and 81-1h samples, respectively. In view of the same pyrolysis temperature and same carbon precursor being used for both samples, no major differences in this ratio are to be expected[51]. However, the slight difference may indicate a higher disorder degree for sample 81-1h than for 88-3h. Furthermore, both materials exhibit a tiny and broad Raman band at 460 cm^{-1}, which further confirms the presence of amorphous nanosilicon. Previous works have reported that the center frequency of the peak attributed to the Si-Si transverse optical (TO) band at approximately 521 cm^{-1} for bulk silicon shifts towards smaller energies with decreasing particle diameter (due to the phonon confinement effect), showing an asymmetric broadening band[45,52].

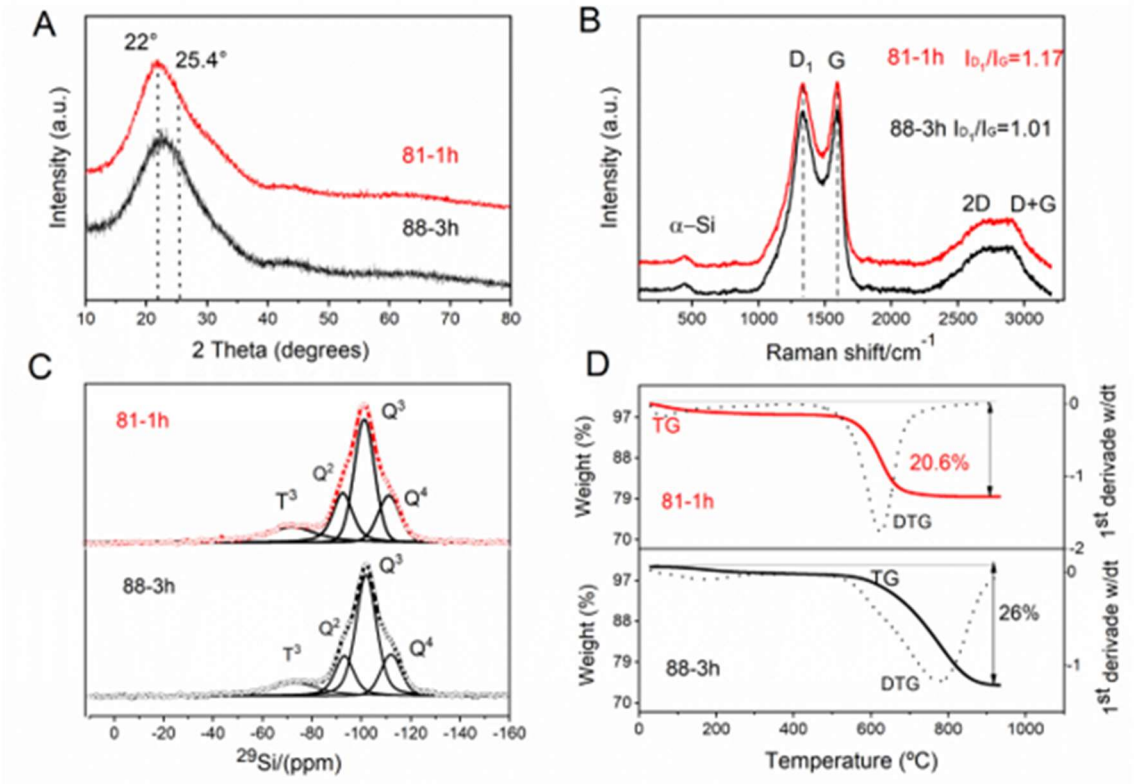

Figure 2. XRD pattern (A), Raman spectra (B), ^{29}Si CPMAS NMR spectra (C) and thermogravimetric analyses of the (D) NC-SiOC 81-1h and 88-3h samples pyrolyzed in air. TGA was performed under flowing synthetic air at a heating rate of 10 °C/min.

To elucidate the sample composition, the silicon tetrahedral species were examined by ^{29}Si CPMAS NMR. In both samples, Q^4 (Si $(-OSi)_4$), Q^3 (Si $(-OSi)_3(OH)$), Q^2 (Si $(-OSi)_2(OH)_2$), and T^3 ($CSi(OSi)_3$) species were observed at -112, -101, -93, and -72 ppm, respectively[53,54]. No spectral features associated with the tetrahedral structures of SiO_2C_2 (-22 ppm), SiC_4 (-18 ppm), and SiC_3O (+6.7 ppm) were observed[53,55]. The presence of metallic silicon forming $Si(Si_4)$ units (-80 ppm) is uncertain due to overlap with the Q^2 and T^3 peaks[56,57].

To estimate the thermal stability of both samples, thermogravimetric analysis (TGA) and the derivative thermogravimetry (DTG) curves were obtained in an air atmosphere (Table 1 and Fig. 2D). The thermograms show an initial weight loss of approximately 3 wt. % below 200 °C, most likely due to the evaporation of adsorbed water. It is observed that the onset of the oxidation of sample 81-1h occurs at a lower temperature, 462 °C relative to 530 °C for 88-3h, and the maximum rate of oxidation (DTG peak) is shifted from approximately 620 °C to 780 °C for 88-3h. These two facts demonstrate that sample 81-1h has a lower resistance to oxidation than 88-3h. The weight loss of

21% for 81-1h and 26% for 88-3h between 500 and 950 °C is mostly associated with the combustion of the free carbon phase [58].

The elemental analysis (EA) (Table 1) clearly indicates that the synthesis conditions explored here allow for materials with varied nitrogen-doped carbon compositions. The sample synthesized using an equal APTES to citrate ratio (88-3h) shows a 38% higher content of carbon, 55% more nitrogen, and 20% more silicon than the 81-1h sample. Interestingly, the amount of oxygen in the sample with a higher APTES molar content (81-1h) is 35% higher. Nitrogen isotherm adsorption/desorption data and Barrett-Joyner-Halenda (BJH) pore volumes are summarized in Table 1. A BET specific surface area of 33 m^2/g was obtained for 81-1h samples (see Fig. S3 of the Supplementary info). Conversely, for 88-3h, the nonporous features evidenced in the SEM micrographs were further confirmed by the low BET SSA of < 5 m^2/g obtained. In 81-1h, both mesopores and macropores exist with an average size of approximately 20-150 nm.

Table 1. Elemental analysis of data measured by TGA and BET analysis of pyrolyzed NC/SiOC.

Sample NC/SiOC	Elemental analysis Wt. %					Empirical formula	TGA		BET Surface area (m^2/g)	Pore width (nm)
	%C	%Si*	%O	%N	%H		Weight loss	residue		
81-1h	14.8	30.7	53	0.86	0.6	$SiC_{1.13}O_{3.04}$	20.6	79.4	33	20-150
88-3h	23.9	38.6	35.2	1.93	0.4	$SiC_{1.45}O_{1.60}$	26	74	< 5	-

*Silicon percentage obtained from the difference. Empirical formula normalized to one silicon atom.

Fig. 3 displays scanning transmission electron microscopy (STEM), electron diffraction spectroscopy (EDS), and X-ray photoelectron spectroscopy data. EDS elemental mapping shows a qualitative description of the sample composition; silicon, oxygen, carbon, and nitrogen were present throughout the entire cross-section of the particles (Fig. 3A-E). Similarly, the XPS survey spectra (Fig. S4) show the C 1*s* peak at 284.4 eV, O 1*s* peak at 532.3 eV, Si 2*p* peak at 100.3 eV, and N 1*s* peak at 399.5 eV, respectively, with no evidence of impurities. The surface elemental composition determined from XPS was determined to be C=33.8 at% (23.8 wt.%), O=45.8 at% (43.1 wt.%), N=0.7 at% (0.58 wt.%) and Si=19.7 at% (32.51 wt.%) for sample 81-1h, while

the bulk elemental analysis obtained by the inert gas fusion technique (Table 1) showed a composition of C= 19.5 at% (14.8 wt.%), O=52.5 at% (53 wt.%), N=0.97 at% (0.86 wt.%) and Si=17.3 at% (30.7 wt.%). These differences may be a consequence of the native silicon oxide layer since neither etching nor argon sputtering depth profiling was realized before XPS analysis. Furthermore, according to the structural nanodomain model for SiOC[18,59] in hybrid materials, such as those synthesized here, certain phase segregation can take place, and thus, variation along the sample can be expected.

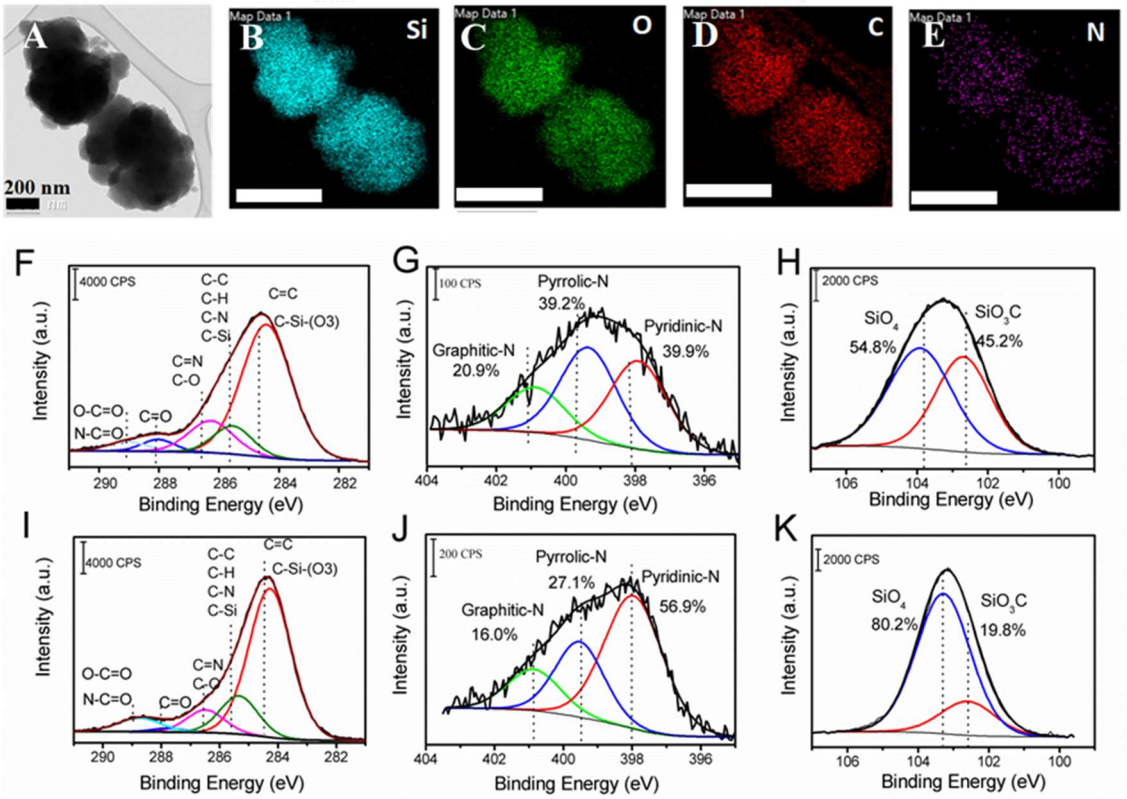

Figure 3. TEM image of NC-SiOC 81-1h (A); STEM-EDS mapping showing the distribution of elements in image (A). Silicon (B); oxygen (C); carbon (D), and nitrogen (E). The length of the scale bar is 500 nm. Fitted XPS spectra curve of pyrolyzed N-doped C/SiOC samples: 81-1h (F-H) and 88-3h (I-K). C 1s (F and I), N 2s (G and J), Si 2p (H and K) spectra.

The high-resolution C 1*s* spectra of both samples (Fig. 3F and 3I) show a major peak at approximately 284.4 eV, assigned to C=C sp^2 and C-Si(-O_3). At higher binding energies, the contribution of the oxygen and nitrogen atoms bonded to C, such as C-C sp^3 (associated with C-N, C-H, C-Si, and C-O-Si bonding), C (epoxy), and C=N, C=O and N-C=O[9,43,60], was observed. The relative contribution of each bond assigned in the spectra is shown in Table S1 (Supplementary info). The most predominant peak corresponds to the overlapping of the bonding energy of sp^2 carbon and C-Si(-O_3), with

percentages of the area of approximately 67 and 68% for samples 81-1h and 88-3h, respectively. The content of C=O groups (288 eV) and the peak associated with C-O and C=N at 236.3 eV for sample 81-1h are larger than those for 88-3h, which agrees with the higher amount of oxygen in 81-1h than in 88-3h, as shown in Table 1.

The XPS spectra of nitrogen show that nitrogen-doped carbon structures are present in both cases (Figs. 3G and 3J). The spectra were curve-fitted with three peaks assigned to pyridinic N (two C-N bonds in a hexagon) at 398 eV, pyrrolic N (two C-N bonds in a pentagon) at 399 eV and graphitic N (three sp^2 C-N bonds) at 400.7 eV[61–63]. The relative nitrogen composition obtained by curve fitting show that pyrrolic N and pyridinic N are the main species formed in both samples (approximately 78% in 81-1h and 70% in 88-3h), while graphitic N shows a contribution lower than 30%. Pyridinic N and graphitic N have been reported as efficient Li intercalation sites[61]. Specifically, pyridinic N has been related to higher values of reversible capacity[64]. Pyrrolic N has been reported to be less favorable than pyridinic N in terms of lithium storage[65]. In general, it is widely accepted that both pyridinic and pyrrolic nitrogen create additional defects and greater disorder within the graphene lattice, while graphitic N increases the electron density within the delocalized π-system[66].

The Si 2*p* high-resolution spectra (Figs. 3H and 3K) display two peaks at approximately 102.5 eV and 103.3 eV assigned to Si^{+3} (SiO_3C) and Si^{+4} (SiO_4) phases[9,37,67,68], which are also in line with those observed in ^{29}Si NMR. A shift of +0.6 eV was also noticed for Si^{4+} in the 81-1h sample, which could be associated with differences in the oxide thickness[69,70]. Comparison between the curve-fitted peaks reveals a significant increase in the content of SiO_3C species (~43.7%) in sample 81-1h, which could be related to its higher APTES:citrate molar ratio, suggesting that most of the APTES SiO_3C units are retained. The absence of Si is also noticeable (with a Si^0 2p peak binding energy of 99.0 eV)[68]. However, since the synthesis of NC/SiOC materials reported here was inspired by the synthesis of silicon and nitrogen-graphene quantum dots, some amorphous silicon nanoparticles can be expected. In any case, these results reflect that more in-depth studies about the silicon environment deserve to be done. Similar to what was described, the Si environment observed by XPS may be affected by the SiO_2 native layer that can produce differences from the bulk. Although it is a common practice to reduce surface oxides and other contaminants by sputter cleaning with Ar^+ ions to obtain a pristine surface prior to XPS analysis, in the case of the

NC/SiOC samples, this procedure was avoided to diminish the risk of modifying the surface structure and composition of the C-N compounds, which can be significantly affected [71–73].

The fact that the nitrogen content increases when both a longer reaction time and a similar APTES:citrate molar ratio are used suggests that carbon structures can be formed according to the mechanism proposed for the formation of nitrogen-doped graphene-like structures[30]. This mechanism is based on the reaction of the amine group in APTES with -COOH groups from citric acid forming an amide linkage. In the first stage, the amine works as a base to facilitate condensation with the release of water in citric acid. Then, citric acid molecules self-assemble into sheet structures, followed by a condensation reaction through intermolecular dehydroxylation to give an N-enriched graphene framework [30].

Based on the APTES molecular structure, it can be assumed that part of the nitrogen atoms condensed in the carbonaceous structure may still be bonded to the SiO_3C tetrahedral structure through the propyl alkyl chain. After pyrolysis at 1000 °C, it can be expected that the obtained free carbon is formed from the alkyl chain as well as the nitrogen-doped carbonaceous structure. At the same time, the silanol groups of APTES form a polymeric network based on Si-O linkages in which certain SiO_3C units remain in the hybrid materials.

Note that contrary to the observations made for sample 81-1h, the TGA weight loss at 950 °C for sample 88-3h corresponds to the sum of the percentages of C, N and H obtained by EA, as shown in Table 1. This fact may indicate that 81-1h contains more oxygen groups that can be part of the nitrogen-doped carbonaceous phase than 88-3h. Based on the abovementioned mechanism, it can be expected that the more extensive the carbon condensation reaction is, the lower the content of oxygenated moieties, since dehydrolysis and dehydroxylation reactions take place.

The absence of nano-/mesoporosity in 88-3h may be associated with rearrangement at the molecular and nanoscale levels through the formation of highly condensed structures with high resistance to oxidation[10]. Although a relationship has been established between the formation of C-N bonds (while decreasing the amount of C-OH and C-O moieties) and the higher thermal resistance[74], we believe that the high thermal stability observed may be related to the distribution of the SiO_2 phase. It has

been reported previously that when SiO_2 is formed on the surface of SiOC, it can act as a protective layer, hindering oxygen diffusion into the particle, and thus, the SiOC network largely remains stable[75]. This fact was evidenced in the SEM images of both samples after TGA measurements were performed in air (Fig. S5 of the Supplementary info). The surface of sample 88-3h remains almost flat and inert, with only minor cracks. In the case of sample 81-1h, although no information about cracks can be obtained, having smaller sphere-like particles could facilitate the evolution of the formed gases more easily.

3.2 Electrochemical performance

Figure 4 shows the potential profiles of both electrodes from the first to the third galvanostatic charge/discharge cycles (Fig 4A and 4B) and the corresponding differential capacity curves (Figures 4C and 4D) performed at 0.1 A/g between 0.05 and 2.5 V. For the first cycle using the pyrolyzed 81-1h and 88-3h samples as active materials (Fig 4A and 4B), the charge capacity reached 622 and 367 mAh/g, respectively. In the subsequent cycles, the capacity values of both samples remain almost constant. Both electrodes commonly show a characteristic shoulder at approximately 0.7 V and a flat plateau at approximately 0.18 V during the first discharge step (lithiation). In the second and subsequent insertion curves, no clear plateaus were observed. The minor shoulder can be associated with the reaction between Li^+ and acetylene black carbon used for the composite[56] and with the formation of solid electrolyte interface (SEI)[76], while the capacity of the potential region lower than 0.5 V may reflect SiOC/SiOx lithiation[77], lithium absorption into the turbostratic nitrogen-doped carbon structure[14,15] and electrolyte decomposition[78]. Specifically, from the first differential capacity dQ/dV response, where Q is capacity and V voltage, a strong reductive peak at 0.18 V versus Li/Li^+ corresponds to the above-mentioned plateau and can be associated mainly to irreversible reactions of from SiOx to elemental silicon [76], while the peaks in the range of ~ 0.08-0.12 are related to the formation of the a-Li_xSi phases [79]. The charge process shows a tiny shoulder at around 0.32-0.45 V vs. Li/Li^+ that can presumably be related to both Li alloy/dealloy with amorphous silicon domains formed during the first cycle [80] and to Li-ion insertion/extraction from the Si-O network in SiOC[81]. In the second and third

cycles (enlarged dQ/dV profiles in Fig 1C and 1D) the discharge and charge processes show shoulders at around 0.5 V and 0.32-0.45 V vs. Li/Li^+, respectively, indicating that after the first cycle, the electrochemical reactions that take place are similar to those of amorphous silicon[80]. It is also noticed much higher electrochemical activity in the sphere-like sample 81-1h than that of 88-3h, in line with the delithiation capacity observed.

Figure 5 shows the rate capability test results (delithiation capacity vs. cycle number) of both half-cells at current densities from 0.1 to 2.4 A/g. It is noticeable that the average delithiation capacity of the 81-1h sample at 0.1 A/g is approximately 40% higher than the capacity of sample 88-3h. This difference in the electrochemical performance is maintained even when the current density is increased to 0.2 A/g or higher.

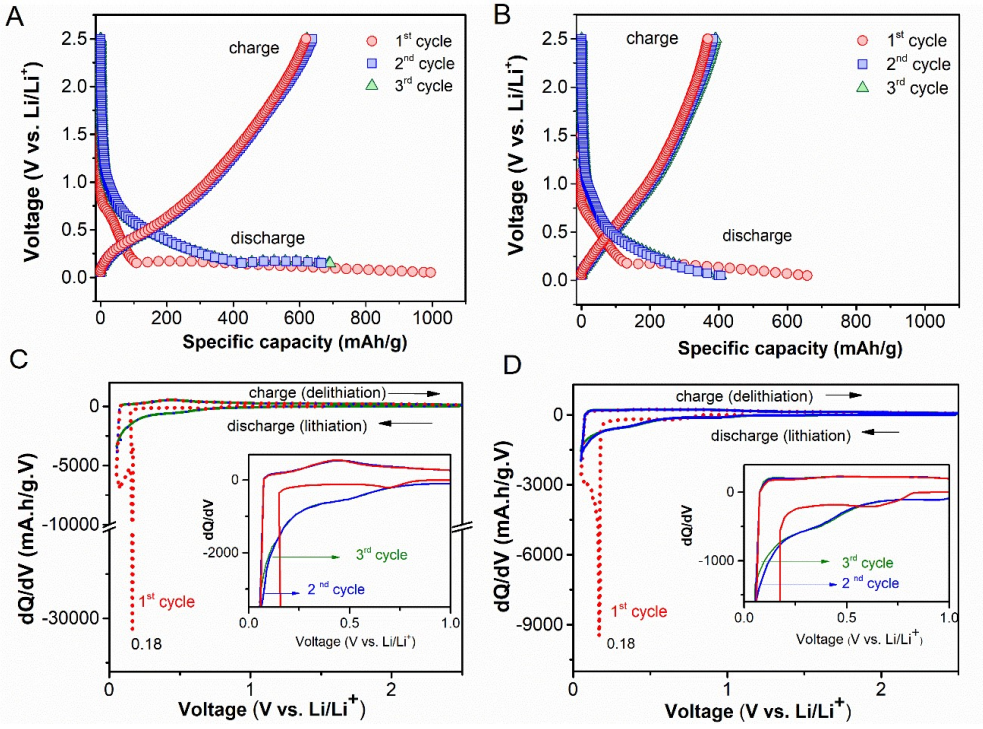

Figure 4. Discharge/charge voltage profile and differentiated capacity curves (dQ/dV vs. voltage) during the cycling of 0.1 A/g of NC-SiOC materials with PAA as a binder and EC/DEC with a ratio of 50:50 as the organic solvent, and 1 M $LiPF_6$ as the electrolyte: 81-1h (A and C) and 88-3h electrodes (B and D). Testing voltage window was from 0.05 V to 2.5 V. The insets of C and D are magnification in the range of 0 V to 1 V vs Li/Li^+.

After 30 cycles, when the current is returned back to 0.1 A/g, the recovered capacity is approximately 90 and 97% for 81-1h and 88-3h, respectively. Then, both samples were

tested by performing 1000 cycles at 1.6 A/g to determine their long-term cycling stability. Subsequently, from cycles 1035 to 1055, the current density was brought back to 0.1 A/g to evaluate the recovered capacity of both active materials. In Fig. 5B, it is observed that during the whole test, sample 81-1 shows a higher capacity, while 88-3h has a higher recovery after 1055 cycles. The observed delithiation capacities are 559 and 354 mAh/g in the 35th cycle and 426 and 349 mAh/g in the 1055th cycle; thus, the recovered capacities obtained are 73 and 98% for samples 81-1h and 88-3h, respectively.

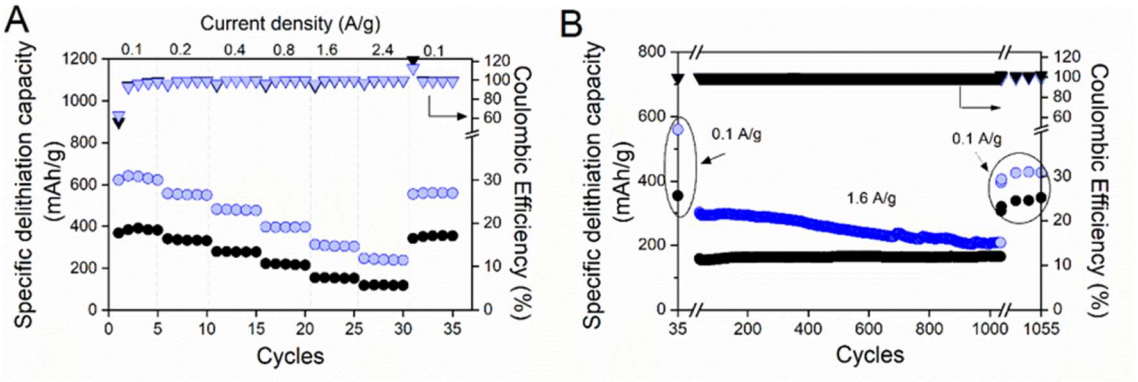

Figure 5. Electrochemical performance of the NC-SiOC materials with PAA as a binder, EC/DEC at a 50:50 ratio as the organic solvent, and 1 M $LiPF_6$ as the electrolyte with cycling between 0.05 and 2.5 V vs. *Li/Li^+. Filled black circles represent the data for 88-3h, and clear blue circles represent the data for 81-1h. Delithiation capacity is represented by circle symbols; Coulombic efficiency is represented by triangles. Charge/discharge: (A) specific capacity and Coulombic efficiency as a function of cycle number for the composite electrode cycled at 0.1 A/g and 1000 cycles at 1.6 A/g (B). The capacity values are reported per mass of the active material.*

Although the lithium insertion mechanism in SiOC/SiOx is still a matter of debate, in the materials synthesized here, it can be assumed that the main active sites in the glassy phase are provided by SiO_4 and SiO_3C tetrahedral units, and probably also in amorphous silicon. Since the reactions for lithium-ion extraction/insertion in oxycarbides are not well established, some of the possible reactions based on the SiO_2 reaction with Li^+ for the formation of Li*x*Si alloys, lithium silicates (Li_4SiO_4, $Li_6Si_2O_7$, Li_2SiO_3) and Li_2O would be as follows [18]·[82].

$$4Li^+ + 4e^- + SiO_2 \rightarrow 2\,Li_2O + Si \qquad (1)$$

$$4Li^+ + 4e^- + 2SiO_2 \rightarrow Li_4SiO_4 + Si \qquad (2)$$

$$Si + xLi^+ + xe^- \leftrightarrows Li_x\text{Si} \quad (3)$$

In the case of the carbonaceous phase, the free carbon is composed mainly of disordered carbon, as was observed in the Raman spectra. In graphitic structures, the lithium storage mechanism is based on intercalation/deintercalation, in which each Li is associated with 6 carbon atoms, giving a maximum lithium storage capacity of 372 mAh/g. In the case of disordered carbon, Li insertion occurs by adsorption and surface storage since topological defects create a large number of surface active sites or cavities, which can accommodate extra Li ions[14,43]. Thus, in highly disordered materials, morphological aspects, such as voids, micro-/mesoporosity, particle size and the defects such as those generated by heteroatoms, become relevant.

The observed superior performance in terms of the capacity and initial Coulombic efficiency of sample 81-1h can be correlated to morphology and compositional features. First, the more disordered carbon allows for a higher capacity to store lithium, not only between the sp^2 C layers but also at the edge of the layers[13]. Second, the higher electrolyte-electrode area and the presence of macro- and mesopores in the sphere-like sample can be favorable in terms of Li^+ diffusion into the inner region of the particles[83,84]. Similarly, a higher surface area may imply that the active sites provided by both the glassy-phase and N-doped carbonaceous phases are more available for Li insertion/extraction. These findings are consistent with previous reports in which sphere-like oxycarbides show better performance than bulk particles[81,85]. Note that neither acid/base catalysts[85] nor templates[81] were used to obtain the sphere-like silicon oxycarbide particles reported here.

As shown in Fig. 4, the initial Coulombic efficiency is higher for 81-1h (~63%) than for 88-3h (~55%). Although the charge consumption in the reduction of the electrolyte and the formation of a solid electrolyte interphase (SEI) may have a certain contribution to the irreversibility, it is believed that the glassy composition plays an important role[86]. It is commonly reported that the formation of irreversible phases such as lithium oxide (Li_2O) and lithium silicates (Eq 1-2) is favorable in oxygen-rich SiO_x materials.

Thus, it is clear that this phenomenon alone cannot explain the fact that sample 81-1h has 35% more oxygen than 88-3h, showing a lower irreversible capacity. We attribute the higher reversibility obtained in 81-1h to the more SiO_3C units present, which has been recognized to provide reversible sites. In contrast, in 88-3h predominant SiO_4 sites

may produce both irreversible (Li_4SiO_4) and reversible products (Li_2SiO_3), as was reported previously[56]. On the other hand, the XPS data revealed that pyridinic N is predominantly formed in sample 88-3h. Although this structure is considered to be highly reversible [64], the small surface area and porosity of this sample may make these sites inaccessible to lithium ions.

In the long charge/discharge cycling life (Fig. 5B), in the case of sample 81-1h, no capacity changes were observed until approximately 300 cycles at 1.6 A/g. After this, the capacity of the sample decayed to 208 mAh/g at the 1000^{th} cycle. Conversely, in sample 88-3h its capacity remained constant at 165 mAh/g. From the 1035^{th} cycle to the 1055^{th} cycle, when the current returns to 0.1 A/g, the capacity obtained was 340 mAh/g, meaning that in a total of 1055 cycles, the capacity decay was only 13%. Such high stability reflects that the active sites for Li insertion/extraction remain almost unaltered and reflects the outstanding response of the material under stress conditions.

After Li_xSi and lithium silicate formation, phase segregation occurs, and the silicate surrounds the silicon alloy, exerting a buffer effect[86]. In the case of the carbonaceous structure, the strength of C in the N-doped graphene-like structure may form a stable backbone structure that helps to support volume changes in the material. We believe that the remarkable long-term charge–discharge cycling of sample 88-3h can be associated with both the increased formation of lithium silicate and its higher C content since both can contribute to reducing stresses upon cycling[16,87]. The origin of the decay in sample 81-1h is not yet clear; perhaps the amount of nitrogen-carbon is not enough to support the continuous volume variation.

In general, the reversible capacity and ICE of NC-SiOC 81-1h are higher than those of some other SiOC-carbon rich materials[12,88,89] (Table S2), even when, in our case, a cutoff of 0.05 V was used. Similarly, in comparison with SiOC/composites such as SiOC/graphene or N-C fiber composites, our material is quite competitive in terms of delithiation capacity. In fact, in terms of long-term cycling at a high rate (1000 cycles at 1600 mA/g), our results are only comparable with ref. [9] since these cycling conditions are not conventionally tested in SiOC materials. Regarding state-of-the-art graphite, previous works have shown that a fast charging process with a low operating voltage versus Li/Li^+ results in the generation of lithium dendrites or plating, leading to serious safety issues[90,91]. In addition, graphite has shown rapid capacity fade at current densities higher than 1C[90]. In fact, at 2C rates (~700 mA/g), the performance of

graphite further deteriorates, giving only 12% of its theoretical capacity[92]. Therefore, the promising results obtained with NC/SiOC in this work promote this material as an alternative to conventional graphite negative electrodes.

Importantly, this result suggests that the synthesis conditions explored here can be tailored to obtain hybrid materials with the best characteristics of each condition: high capacity, as shown in 81-1h, and stability during long-term cycling at high current density, as is the case for sample 88-3h. NC materials synthesized by using in-between conditions will be the subject of future work.

3.2.1 Nitrogen-doped carbon

In both materials, the nitrogen-doped structures may generate additional structural defects that promote lithium insertion sites and rapid charge-transfer reactions[65,93]. The nitrogen amount obtained from the elemental analysis was 0.97 wt. % (0.74 at. %) and 2.26 wt. % (1.17 at. %) for 81-1h and 88-3h, respectively. Although this content is relatively low, some contribution to the enhanced electrochemical activity can be expected since nitrogen doping levels as low as ~1-2 at. % in CNTs and graphene nanosheets have shown better electrochemical activity than similar undoped material[64]

The low nitrogen content could be an effect of the high temperature of pyrolysis[94]. However, other factors, such as reaction time, may also have important contributions. In the synthesis of materials for bioimaging or immunofluorescence applications, the relationship between nitrogen-related surface states and emission properties is an important issue that has been extensively explored[95,96]. For instance, at temperatures from 150 °C to 180 °C, the relative fraction of pyridinic-N and pyrrolic-N decreased since these sites are converted to graphitic N. Even if the study of the evolution of the N sites and the effect of the pyrolysis temperature was beyond the scope of this research, our results nonetheless highlight the fact that both this novel synthesis method and application deserve to be explored more deeply.

Moreover, note that this synthesis method is more advantageous than elaborate procedures or multistep processes[29,97]. In addition, the fact that low-cost sodium citrate and glycerol are used represent an additional advantage in terms of cost and environmental issues, as both are nontoxic, and glycerol is considered an eco-friendly solvent[98].

3.2.2 Electrolyte-PAA interface

Electrode performance highly depends on the selected binder. According to previous reports, poly(acrylic)acid showed better performance than binders such as poly(vinylidene fluoride) (PVDF), poly(vinyl alcohol) (PVA) and carboxymethyl cellulose (CMC) in active materials such as SiO[99], graphite[100], and silicon nanoparticles[7,101]. Considering the hybrid features of NC-SiOC, a strong interaction between carboxylate groups from PAA and hydroxyl groups on the SiO_2/SiOC surface, similar to a previous report for SiO/PAA composites[99], is expected.

The excess oxygen atoms in sample 81-1h can improve the binder-active material interaction. In electrode preparation, PAA, carbon black, and the active material are mixed in ethanol; thus, higher wettability in an oxygen-rich NC/SiOC 81-1h would be expected. A similar finding has been reported in porous carbon with a high content of C-O species as well as in nitrogen/oxygen-codoped mesoporous carbon[83,102]. In addition, most of the oxygen might not be available to contact the electrolyte and lithium ions since they are already interacting with -COOH moieties from PAA. Our explanation is consistent with the work of Komaba et al.[99], who observed that SiO particles are uniformly covered by PAA polymer unlike the poly(vinylidene fluoride) PVDF binder, which is one of the most common binders used in SiOC/SiOx materials[83,102].

On the other hand, the interaction between the N-doped graphene-like phase and PAA may be similar to that previously reported for graphite/PAA electrodes, in which the formed SEI layer between the negative polarized oxygen atoms from PAA and the carbonate-based electrolyte may interact with the solvated lithium ions to accelerate the lithium desolvation. Consequently, the lithium intercalation into the graphite layer could be highly favorable. In others words, PAA acts not only as a binder but also as a coating, showing a similar function to the artificial solid-electrolyte interphase[100].

4. Conclusions

We have demonstrated that APTES, citrate, and glycerol can be used for the formation of a hybrid material, N-doped carbon/SiOC. This synthesis is more advantageous than elaborate procedures or multistep processes and opens the door for using similar procedures already developed for the synthesis of quantum dots, in which N-doping mechanisms and experimental conditions have been studied extensively. The sphere-

like NC-SiOC material with a larger surface area and mainly composed of SiO_3C units shows delithiation capacity values up to 2 times higher than those reported for graphite. In terms of stability and recovery capacity, the sample with the larger amount of carbon and more N atoms shows better electrochemical performance: 98% recovery capacity over 1000 cycles at 1.6 A/g is among the highest value reported in the literature for similar materials.

Funding

This work was supported by CNPq, CAPES, FAPESP (2015/26308-7 and 2020/08553-2) and the Natural Sciences and Engineering Research Council of Canada (Discovery Grant). I. M. wishes to thank FAPESP for fellowship grants (2017/20043-7 and 2019/07638-7). The research infrastructures of nanoQAM and IQ-USP were used during this work.

Acknowledgment

The authors would like to acknowledge Dr. Galyna Shul, Gwenael Chamoulaud from NanoQAM, and Dr. Peter Hammer for the XPS measurements. I.E.M also thanks Prof. Maraisa Goncalves and MSc. Thaylan Pinheiro Araujo for helpful discussions.

Notes

The authors declare no competing financial interest.

References

[1] R. Schmuch, R. Wagner, G. Hörpel, T. Placke, M. Winter, Performance and cost of materials for lithium-based rechargeable automotive batteries, Nat. Energy. 3 (2018) 267–278. https://doi.org/10.1038/s41560-018-0107-2.

[2] G.E. Blomgren, The Development and Future of Lithium Ion Batteries, J. Electrochem. Soc. 164 (2017) A5019–A5025. https://doi.org/10.1149/2.0251701jes.

[3] Y. Hu, R. Demir-cakan, M. Titirici, J. Müller, R. Schlögl, M. Antonietti, J. Maier, Superior Storage Performance of a Si @ SiO x / C Nanocomposite as Anode Material for Lithium-Ion Batteries, Angew. Chemie Int. Ed. 47 (2008) 1645–1649. https://doi.org/10.1002/anie.200704287.

[4] D. Ahn, R. Raj, Cyclic stability and C-rate performance of amorphous silicon and carbon based anodes for electrochemical storage of lithium, J. Power Sources. 196 (2011) 2179–2186. https://doi.org/10.1016/j.jpowsour.2010.09.086.

[5] H.F. Andersen, C.E.L. Foss, J. Voje, R. Tronstad, T. Mokkelbost, P.E. Vullum, A. Ulvestad, M. Kirkengen, J.P. Mæhlen, Silicon-Carbon composite anodes from industrial battery grade silicon, Sci. Rep. 9 (2019) 1–9. https://doi.org/10.1038/s41598-019-51324-

4.

[6] B.D. Assresahegn, D. Bélanger, Synthesis of binder-like molecules covalently linked to silicon nanoparticles and application as anode material for lithium-ion batteries without the use of electrolyte additives, J. Power Sources. 345 (2017) 190–201. https://doi.org/10.1016/j.jpowsour.2017.01.135.

[7] N. Sanchez-Ramirez, B.D. Assresahegn, R.M. Torresi, D. Bélanger, Producing high-performing silicon anodes by tailoring ionic liquids as electrolytes, Energy Storage Mater. 25 (2020) 477–486. https://doi.org/10.1016/j.ensm.2019.09.035.

[8] T. Chen, J. Wu, Q. Zhang, X. Su, Recent advancement of SiOxbased anodes for lithium-ion batteries, J. Power Sources. 363 (2017) 126–144. https://doi.org/10.1016/j.jpowsour.2017.07.073.

[9] L. David, R. Bhandavat, U. Barrera, G. Singh, Silicon oxycarbide glass-graphene composite paper electrode for long-cycle lithium-ion batteries, Nat. Commun. 7 (2016) 1–10. https://doi.org/10.1038/ncomms10998.

[10] Q. Wen, Z. Yu, R. Riedel, The fate and role of in situ formed carbon in polymer-derived ceramics, Prog. Mater. Sci. 109 (2020) 100623. https://doi.org/10.1016/j.pmatsci.2019.100623.

[11] J.R. Dahn, Method for forming a SiOC ceramic electrode material and rechargeable lithium ion battery containing same as an anode, 1998. https://doi.org/10.1136/jnnp.56.1.40.

[12] M. Wilamowska-Zawlocka, P. Puczkarski, Z. Grabowska, J. Kaspar, M. Graczyk-Zajac, R. Riedel, G.D. Sorarù, Silicon oxycarbide ceramics as anodes for lithium ion batteries: Influence of carbon content on lithium storage capacity, RSC Adv. 6 (2016) 104597–104607. https://doi.org/10.1039/c6ra24539k.

[13] M. Graczyk-Zajac, D. Vrankovic, P. Waleska, C. Hess, P.V. Sasikumar, S. Lauterbach, H.J. Kleebe, G.D. Sorarù, The Li-storage capacity of SiOC glasses with and without mixed silicon oxycarbide bonds, J. Mater. Chem. A. 6 (2017) 93–103. https://doi.org/10.1039/c7ta09236a.

[14] J.R. Dahn, T. Zheng, Y. Liu, J.S. Xue, Mechanisms for lithium insertion in carbonaceous materials, Science (80-.). 270 (1995) 590–593. https://doi.org/10.1126/science.270.5236.590.

[15] J. Kaspar, M. Graczyk-Zajac, R. Riedel, Determination of the chemical diffusion coefficient of Li-ions in carbon-rich silicon oxycarbide anodes by electro-analytical

methods, Electrochim. Acta. 115 (2014) 665–670. https://doi.org/10.1016/j.electacta.2013.10.184.

[16] H. Sun, K. Zhao, Atomistic Origins of High Capacity and High Structural Stability of Polymer-Derived SiOC Anode Materials, ACS Appl. Mater. Interfaces. 9 (2017) 35001–35009. https://doi.org/10.1021/acsami.7b10906.

[17] M. Wilamowska, V.S. Pradeep, M. Graczyk-Zajac, R. Riedel, G.D. Sorarù, Tailoring of SiOC composition as a way to better performing anodes for Li-ion batteries, Solid State Ionics. 260 (2014) 94–100. https://doi.org/10.1016/j.ssi.2014.03.021.

[18] Z. Liu, Q. Yu, Y. Zhao, R. He, M. Xu, S. Feng, S. Li, L. Zhou, L. Mai, Silicon oxides: A promising family of anode materials for lithium-ion batteries, Chem. Soc. Rev. 48 (2019) 285–309. https://doi.org/10.1039/c8cs00441b.

[19] H. Konno, T. Morishita, C. Wan, T. Kasashima, H. Habazaki, M. Inagaki, Si-C-O glass-like compound/exfoliated graphite composites for negative electrode of lithium ion battery, Carbon N. Y. 45 (2007) 477–483. https://doi.org/10.1016/j.carbon.2006.11.002.

[20] R. Bhandavat, G. Singh, Stable and efficient li-ion battery anodes prepared from polymer-derived silicon oxycarbide-carbon nanotube shell/core composites, J. Phys. Chem. C. 117 (2013) 11899–11905. https://doi.org/10.1021/jp310733b.

[21] Y. Li, Y. Hu, Y. Lu, S. Zhang, G. Xu, K. Fu, S. Li, C. Chen, L. Zhou, X. Xia, X. Zhang, One-dimensional SiOC/C composite nanofibers as binder-free anodes for lithium-ion batteries, J. Power Sources. 254 (2014) 33–38. https://doi.org/10.1016/j.jpowsour.2013.12.044.

[22] Y. Ren, B. Yang, X. Huang, F. Chu, J. Qiu, J. Ding, Intercalated SiOC/graphene composites as anode material for li-ion batteries, Solid State Ionics. 278 (2015) 198–202. https://doi.org/10.1016/j.ssi.2015.06.020.

[23] Y.P. Wu, E. Rahm, R. Holze, Effects of heteroatoms on electrochemical performance of electrode materials for lithium ion batteries, Electrochim. Acta. 47 (2002) 3491–3507. https://doi.org/10.1016/S0013-4686(02)00317-1.

[24] C. Zhang, B. Wang, X. Shen, J. Liu, X. Kong, S.S.C. Chuang, D. Yang, A. Dong, Z. Peng, A nitrogen-doped ordered mesoporous carbon/graphene framework as bifunctional electrocatalyst for oxygen reduction and evolution reactions, Nano Energy. 30 (2016) 503–510. https://doi.org/10.1016/j.nanoen.2016.10.051.

[25] X. Liao, M. Peng, K. Liang, Enhanced electrochemical performance of SiO anode material via nitrogen-doped carbon coating in a facile and green route, J. Electroanal.

Chem. 841 (2019) 79–85. https://doi.org/10.1016/j.jelechem.2019.04.040.

[26] Y. Liang, L. Cai, L. Chen, X. Lin, R. Fu, M.Z. and D. Wu, Silica Nanonetwork Confined in Nitrogen-Doped Ordered Mesoporous Carbon Framework for High-Performance Lithium-Ion Battery Anodes, Nanoscale. 7 (2015) 3971–3975. https://doi.org/https://doi.org/10.1039/C4NR06611A.

[27] T. Mu, P. Zuo, S. Lou, Q. Pan, Q. Li, C. Du, Y. Gao, X. Cheng, Y. Ma, G. Yin, A two-dimensional nitrogen-rich carbon/silicon composite as high performance anode material for lithium ion batteries, Chem. Eng. J. 341 (2018) 37–46. https://doi.org/10.1016/j.cej.2018.02.026.

[28] Y.J. Cho, H.S. Kim, H. Im, Y. Myung, G.B. Jung, C.W. Lee, J. Park, M.H. Park, J. Cho, H.S. Kang, Nitrogen-doped graphitic layers deposited on silicon nanowires for efficient lithium-ion battery anodes, J. Phys. Chem. C. 115 (2011) 9451–9457. https://doi.org/10.1021/jp201485j.

[29] M. Ma, H. Wang, X. Li, K. Peng, L. Xiong, X. Du, Free-standing SiOC/nitrogen-doped carbon fibers with highly capacitive Li storage, J. Eur. Ceram. Soc. 40 (2020) 5238–5246. https://doi.org/10.1016/j.jeurceramsoc.2020.06.034.

[30] D. Qu, M. Zheng, L. Zhang, H. Zhao, Z. Xie, X. Jing, R.E. Haddad, H. Fan, Z. Sun, Formation mechanism and optimization of highly luminescent N-doped graphene quantum dots, Sci. Rep. 4 (2014) 1–11. https://doi.org/10.1038/srep05294.

[31] S. Saire-Saire, E.C.M. Barbosa, D. Garcia, L.H. Andrade, S. Garcia-Segura, P.H.C. Camargo, H. Alarcon, Green synthesis of Au decorated CoFe2O4 nanoparticles for catalytic reduction of 4-nitrophenol and dimethylphenylsilane oxidation, RSC Adv. 9 (2019) 22116–22123. https://doi.org/10.1039/c9ra04222a.

[32] D. Meroni, L. Lo Presti, G. Di Liberto, M. Ceotto, R.G. Acres, K.C. Prince, R. Bellani, G. Soliveri, S. Ardizzone, A close look at the structure of the TiO2-APTES interface in hybrid nanomaterials and its degradation pathway: An experimental and theoretical study, J. Phys. Chem. C. 121 (2017) 430–440. https://doi.org/10.1021/acs.jpcc.6b10720.

[33] N.S.K. Gunda, M. Singh, L. Norman, K. Kaur, S.K. Mitra, Optimization and characterization of biomolecule immobilization on silicon substrates using (3-aminopropyl)triethoxysilane (APTES) and glutaraldehyde linker, Appl. Surf. Sci. 305 (2014) 522–530. https://doi.org/10.1016/j.apsusc.2014.03.130.

[34] L. David, R. Bhandavat, U. Barrera, G. Singh, Silicon oxycarbide glass-graphene composite paper electrode for long-cycle lithium-ion batteries, Nat. Commun. 7 (2016)

1–10. https://doi.org/10.1038/ncomms10998.

[35] M. Wilamowska-Zawlocka, P. Puczkarski, Z. Grabowska, J. Kaspar, M. Graczyk-Zajac, R. Riedel, G.D. Sorarù, Silicon oxycarbide ceramics as anodes for lithium ion batteries: Influence of carbon content on lithium storage capacity, RSC Adv. 6 (2016) 104597–104607. https://doi.org/10.1039/c6ra24539k.

[36] K. Xia, Z. Wu, C. Xuan, W. Xiao, J. Wang, D. Wang, Effect of KOH etching on the structure and electrochemical performance of SiOC anodes for lithium-ion batteries, Electrochim. Acta. 245 (2017) 287–295. https://doi.org/10.1016/j.electacta.2017.05.162.

[37] G.D. Sorarù, G. D'Andrea, A. Glisenti, XPS characterization of gel-derived silicon oxycarbide glasses, Mater. Lett. 27 (1996) 1–5. https://doi.org/10.1016/0167-577X(95)00245-6.

[38] Gelest. A group company of Mitsubishi Chemicals, https://www.gelest.com, Date Accessed 2021-07-09. (n.d.).

[39] Y. Zhong, F. Peng, F. Bao, S. Wang, X. Ji, L. Yang, Y. Su, S.T. Lee, Y. He, Large-scale aqueous synthesis of fluorescent and biocompatible silicon nanoparticles and their use as highly photostable biological probes, J. Am. Chem. Soc. 135 (2013) 8350–8356. https://doi.org/10.1021/ja4026227.

[40] H.-L. Ye, S.-J. Cai, S. Li, X.-W. He, W.-Y. Li, Y.-H. Li, Y.-K. Zhang, One-Pot Microwave Synthesis of Water-Dispersible, High Fluorescence Silicon Nanoparticles and Their Imaging Applications in Vitro and in Vivo, Anal. Chem. 88 (2016) 11631–11638. https://doi.org/10.1021/acs.analchem.6b03209.

[41] K. Xia, Z. Wu, C. Xuan, W. Xiao, J. Wang, D. Wang, Effect of KOH etching on the structure and electrochemical performance of SiOC anodes for lithium-ion batteries, Electrochim. Acta. 245 (2017) 287–295. https://doi.org/10.1016/j.electacta.2017.05.162.

[42] G.D. Sorarù, S. Modena, E. Guadagnino, P. Colombo, J. Egan, C. Pantano, Chemical durability of silicon oxycarbide glasses, J. Am. Ceram. Soc. 85 (2002) 1529–1536. https://doi.org/10.1111/j.1151-2916.2002.tb00308.x.

[43] D. Bhattacharjya, H.Y. Park, M.S. Kim, H.S. Choi, S.N. Inamdar, J.S. Yu, Nitrogen-doped carbon nanoparticles by flame synthesis as anode material for rechargeable lithium-ion batteries, Langmuir. 30 (2014) 318–324. https://doi.org/10.1021/la403366e.

[44] J. Kaspar, M. Graczyk-Zajac, R. Riedel, Carbon-Rich Silicon Oxycarbide (SiOC) and Silicon Oxycarbide / Element (SiOC / X , X = Si , Sn) Nano-Composites as New Anode Materials for Li-Ion Battery Application, Electrochim. Acta. (2014) 1–117.

[45] K. Annou, M. Pelosi, G. Gershinsky, F. Favier, Y. Cuminal, M. Tillard, D. Zitoun, Oxidation pathways towards Si amorphous layers or nanocrystalline powders as Li-ion batteries anodes, Mater. Renew. Sustain. Energy. 3 (2014). https://doi.org/10.1007/s40243-014-0032-7.

[46] M.M. Kadam, O.R. Lokare, K.V.M.K. Kireeti, V.G. Gaikar, N. Jha, Impact of the degree of functionalization of graphene oxide on the electrochemical charge storage property and metal ion adsorption, RSC Adv. 4 (2014) 62737–62745. https://doi.org/10.1039/c4ra08862j.

[47] J. Wu, X. Qin, H. Zhang, Y.B. He, B. Li, L. Ke, W. Lv, H. Du, Q.H. Yang, F. Kang, Multilayered silicon embedded porous carbon/graphene hybrid film as a high performance anode, Carbon N. Y. 84 (2015) 434–443. https://doi.org/10.1016/j.carbon.2014.12.036.

[48] G. Mera, A. Navrotsky, S. Sen, H.J. Kleebe, R. Riedel, Polymer-derived SiCN and SiOC ceramics-structure and energetics at the nanoscale, J. Mater. Chem. A. 1 (2013) 3826–3836. https://doi.org/10.1039/c2ta00727d.

[49] D.G. Henry, I. Jarvis, G. Gillmore, M. Stephenson, J.F. Emmings, Assessing low-maturity organic matter in shales using Raman spectroscopy: Effects of sample preparation and operating procedure, Int. J. Coal Geol. 191 (2018) 135–151. https://doi.org/10.1016/j.coal.2018.03.005.

[50] B. Goffe, J. Petitet, E. Froigneux, M. Moreau, On the characterization of disordered and heterogeneous carbonaceous materials by Raman spectroscopy, 59 (2003) 2267–2276. https://doi.org/10.1016/S1386-1425(03)00070-2.

[51] K. Schutjajew, R. Yan, M. Antonietti, C. Roth, M. Oschatz, Effects of carbon pore size on the contribution of ionic liquid electrolyte phase transitions to energy storage in supercapacitors, Front. Mater. 6 (2019). https://doi.org/10.3389/fmats.2019.00065.

[52] L. Pavesi, Silicon Nanocrystals. Fundamentals, Synthesis and Applications, Wiley-VCH Verlag GmbH & Co. KGaA, 2010.

[53] M.C. Brochier Salon, M.N. Belgacem, Competition between hydrolysis and condensation reactions of trialkoxysilanes, as a function of the amount of water and the nature of the organic group, Colloids Surfaces A Physicochem. Eng. Asp. 366 (2010) 147–154. https://doi.org/10.1016/j.colsurfa.2010.06.002.

[54] L. Pajchel, P. Nykiel, W. Kolodziejski, Elemental and structural analysis of silicon forms in herbal drugs using silicon-29 MAS NMR and WD-XRF spectroscopic methods, J.

Pharm. Biomed. Anal. 56 (2011) 846–850. https://doi.org/10.1016/j.jpba.2011.06.024.

[55] G.T. Burns, R.B. Taylor, Y. Xu, A. Zangvil, G.A. Zank, High-Temperature Chemistry of the Conversion of Siloxanes to Silicon Carbide, Chem. Mater. 4 (1992) 1313–1323. https://doi.org/10.1021/cm00024a035.

[56] X. Liu, Z. Man-Chun, X. Kai, Mechanism of lithium storage in Si-O-C composite anodes, J. Power Sources. 196 (2011) 10667–10672.

[57] G.D. Sorarù, G. D'Andrea, R. Campostrini, F. Babonneau, G. Mariotto, Structural Characterization and High‐Temperature Behavior of Silicon Oxycarbide Glasses Prepared from Sol‐Gel Precursors Containing Si‐H Bonds, J. Am. Ceram. Soc. 78 (1995) 379–387. https://doi.org/10.1111/j.1151-2916.1995.tb08811.x.

[58] L. Wang, K. Lu, Phase development of silicon oxycarbide nanocomposites during flash pyrolysis, J. Mater. Sci. 54 (2019) 6073–6087. https://doi.org/10.1007/s10853-019-03315-z.

[59] C. Stabler, E. Ionescu, M. Graczyk-Zajac, I. Gonzalo-Juan, R. Riedel, Silicon oxycarbide glasses and glass-ceramics: "All-Rounder" materials for advanced structural and functional applications, J. Am. Ceram. Soc. 101 (2018) 4817–4856. https://doi.org/10.1111/jace.15932.

[60] E. Lecoq, D. Duday, S. Bulou, G. Frache, F. Hilt, R. Maurau, P. Choquet, Plasma polymerization of APTEs to elaborate nitrogen containing organosilicon thin films: Influence of process parameters and discussion about the growing mechanisms, Plasma Process. Polym. 10 (2013) 250–261. https://doi.org/10.1002/ppap.201200108.

[61] H. Wang, T. Maiyalagan, X. Wang, Review on recent progress in nitrogen-doped graphene: Synthesis, characterization, and its potential applications, ACS Catal. 2 (2012) 781–794. https://doi.org/10.1021/cs200652y.

[62] M. Inagaki, M. Toyoda, Y. Soneda, T. Morishita, Nitrogen-doped carbon materials, Carbon N. Y. 132 (2018) 104–140. https://doi.org/10.1016/j.carbon.2018.02.024.

[63] C. Maddi, F. Bourquard, V. Barnier, J. Avila, M.C. Asensio, T. Tite, C. Donnet, F. Garrelie, Nano-Architecture of nitrogen-doped graphene films synthesized from a solid CN source, Sci. Rep. 8 (2018) 1–13. https://doi.org/10.1038/s41598-018-21639-9.

[64] H. Wang, C. Zhang, Z. Liu, L. Wang, P. Han, H. Xu, K. Zhang, S. Dong, J. Yao, G. Cui, Nitrogen-doped graphene nanosheets with excellent lithium storage properties, J. Mater. Chem. 21 (2011) 5430–5434. https://doi.org/10.1039/c1jm00049g.

[65] J. Ou, Y. Zhang, L. Chen, Q. Zhao, Y. Meng, Y. Guo, D. Xiao, Nitrogen-rich porous carbon derived from biomass as a high performance anode material for lithium ion batteries, J. Mater. Chem. A. 3 (2015) 6534–6541. https://doi.org/10.1039/c4ta06614f.

[66] A. Gomez-Martin, J. Martinez-Fernandez, M. Ruttert, M. Winter, T. Placke, J. Ramirez-Rico, An electrochemical evaluation of nitrogen-doped carbons as anodes for lithium ion batteries, Carbon N. Y. 164 (2020) 261–271. https://doi.org/10.1016/j.carbon.2020.04.003.

[67] L. Qian, J. Le Lan, M. Xue, Y. Yu, X. Yang, Two-step ball-milling synthesis of a Si/SiOx/C composite electrode for lithium ion batteries with excellent long-term cycling stability, RSC Adv. 7 (2017) 36697–36704. https://doi.org/10.1039/c7ra06671f.

[68] P.M. Dietrich, S. Glamsch, C. Ehlert, A. Lippitz, N. Kulak, W.E.S. Unger, Synchrotron-radiation XPS analysis of ultra-thin silane films: Specifying the organic silicon, Appl. Surf. Sci. 363 (2016) 406–411. https://doi.org/10.1016/j.apsusc.2015.12.052.

[69] O. Sublemontier, C. Nicolas, D. Aureau, M. Patanen, H. Kintz, X. Liu, M.A. Gaveau, J.L. Le Garrec, E. Robert, F.A. Barreda, A. Etcheberry, C. Reynaud, J.B. Mitchell, C. Miron, X-ray photoelectron spectroscopy of isolated nanoparticles, J. Phys. Chem. Lett. 5 (2014) 3399–3403. https://doi.org/10.1021/jz501532c.

[70] K. Joong Kim, K.T. Park, J.W. Lee, Thickness measurement of SiO2 films thinner than 1 nm by X-ray photoelectron spectroscopy, Thin Solid Films. 500 (2006) 356–359. https://doi.org/10.1016/j.tsf.2005.11.042.

[71] N. Hellgren, R.T. Haasch, S. Schmidt, L. Hultman, I. Petrov, Interpretation of X-ray photoelectron spectra of carbon-nitride thin films: New insights from in situ XPS, Carbon N. Y. 108 (2016) 242–252. https://doi.org/10.1016/j.carbon.2016.07.017.

[72] A. Ansón-Casaos, E. Aylón, R. Ríos, J.A. Puértolas, Effects of argon ion sputtering on the surface of graphene/polyethylene composites, Surf. Coatings Technol. 374 (2019) 1059–1070. https://doi.org/10.1016/j.surfcoat.2019.06.091.

[73] L.S. Chang, Y.C. Lin, C.Y. Su, H.C. Wu, J.P. Pan, Effect of C60 ion sputtering on the compositional depth profiling in XPS for Li(Ni,Co,Mn)O 2 electrodes, Appl. Surf. Sci. 258 (2011) 1279–1281. https://doi.org/10.1016/j.apsusc.2011.08.087.

[74] S. Sandoval, N. Kumar, J. Oro-Solé, A. Sundaresan, C.N.R. Rao, A. Fuertes, G. Tobias, Tuning the nature of nitrogen atoms in N-containing reduced graphene oxide, Carbon N. Y. 96 (2016) 594–602. https://doi.org/10.1016/j.carbon.2015.09.085.

[75] K. Lu, D. Erb, M. Liu, Thermal stability and electrical conductivity of carbon-enriched

silicon oxycarbide, J. Mater. Chem. C. 4 (2016) 1829–1837. https://doi.org/10.1039/c6tc00069j.

[76] X. Yang, Z. Wen, X. Xu, B. Lin, S. Huang, Nanosized silicon-based composite derived by in situ mechanochemical reduction for lithium ion batteries, J. Power Sources. 164 (2007) 880–884. https://doi.org/10.1016/j.jpowsour.2006.11.010.

[77] P. Lv, H. Zhao, C. Gao, Z. Du, J. Wang, X. Liu, SiOx-C dual-phase glass for lithium ion battery anode with high capacity and stable cycling performance, J. Power Sources. 274 (2015) 542–550. https://doi.org/10.1016/j.jpowsour.2014.10.077.

[78] M. Gauthier, T.J. Carney, A. Grimaud, L. Giordano, N. Pour, H.H. Chang, D.P. Fenning, S.F. Lux, O. Paschos, C. Bauer, F. Maglia, S. Lupart, P. Lamp, Y. Shao-Horn, Electrode-Electrolyte Interface in Li-Ion Batteries: Current Understanding and New Insights, J. Phys. Chem. Lett. 6 (2015) 4653–4672. https://doi.org/10.1021/acs.jpclett.5b01727.

[79] J. Kaspar, M. Graczyk-Zajac, S. Lauterbach, H.J. Kleebe, R. Riedel, Silicon oxycarbide/nano-silicon composite anodes for Li-ion batteries: Considerable influence of nano-crystalline vs. nano-amorphous silicon embedment on the electrochemical properties, J. Power Sources. 269 (2014) 164–172. https://doi.org/10.1016/j.jpowsour.2014.06.089.

[80] S. Choi, D.S. Jung, J.W. Choi, Scalable fracture-free SiOC glass coating for robust silicon nanoparticle anodes in lithium secondary batteries, Nano Lett. 14 (2014) 7120–7125. https://doi.org/10.1021/nl503620z.

[81] H. Shi, A. Yuan, J. Xu, Tailored synthesis of monodispersed nano/submicron porous silicon oxycarbide (SiOC) spheres with improved Li-storage performance as an anode material for Li-ion batteries, J. Power Sources. 364 (2017) 288–298. https://doi.org/10.1016/j.jpowsour.2017.08.051.

[82] C. Nita, J. Fullenwarth, L. Monconduit, J.M. Le Meins, P. Fioux, J. Parmentier, C. Matei Ghimbeu, Eco-friendly synthesis of SiO2 nanoparticles confined in hard carbon: A promising material with unexpected mechanism for Li-ion batteries, Carbon N. Y. 143 (2019) 598–609. https://doi.org/10.1016/j.carbon.2018.11.069.

[83] C. Yuan, Xianhu Liu, M. Jia, Z. Luo, J. Yao, Facile Preparation of N- and O- Doped Hollow Carbon Spheres Derived from Poly(o-phenylenediamine) for Supercapacitors, J. Mater. Chem. A. (2014). https://doi.org/https://doi.org/10.1039/C4TA06411A.

[84] L. Hua, Q. Chen, Hollow / porous nanostructures derived from nanoscale metal –

organic frameworks towards high performance anodes for lithium-ion batteries, Nanoscale. 6 (2014) 1236–1257. https://doi.org/10.1039/c3nr05192g.

[85] M. Weinberger, C. Pfeifer, S. Schindler, T. Diemant, R.J. Behm, M. Wohlfahrt-Mehrens, Submicron-sized silicon oxycarbide spheres as anodes for alkali ion batteries, J. Mater. Chem. A. 3 (2015) 23707–23715. https://doi.org/10.1039/c5ta06277b.

[86] I. Choi, M.J. Lee, S.M. Oh, J.J. Kim, Fading mechanisms of carbon-coated and disproportionated Si/SiOx negative electrode (Si/SiOx/C) in Li-ion secondary batteries: Dynamics and component analysis by TEM, Electrochim. Acta. 85 (2012) 369–376. https://doi.org/10.1016/j.electacta.2012.08.098.

[87] H. Fukui, Y. Harimoto, M. Akasaka, K. Eguchi, Lithium species in electrochemically lithiated and delithiated silicon oxycarbides, ACS Appl. Mater. Interfaces. 6 (2014) 12827–12836. https://doi.org/10.1021/am502811f.

[88] P. Dibandjo, M. Graczyk-Zajac, R. Riedel, V.S. Pradeep, G.D. Soraru, Lithium insertion into dense and porous carbon-rich polymer-derived SiOC ceramics, J. Eur. Ceram. Soc. 32 (2012) 2495–2503. https://doi.org/10.1016/j.jeurceramsoc.2012.03.010.

[89] M. Graczyk-Zajac, L. Toma, C. Fasel, R. Riedel, Carbon-rich SiOC anodes for lithium-ion batteries: Part I. Influence of material UV-pre-treatment on high power properties, Solid State Ionics. 225 (2012) 522–526. https://doi.org/10.1016/j.ssi.2011.12.007.

[90] C. Mao, R.E. Ruther, J. Li, Z. Du, I. Belharouak, Identifying the limiting electrode in lithium ion batteries for extreme fast charging, Electrochem. Commun. 97 (2018) 37–41. https://doi.org/10.1016/j.elecom.2018.10.007.

[91] B. Writer, Anode Materials, SEI, Carbon, Graphite, Conductivity, Graphene, Reversible, Formation, in: Lithium-Ion Batter. A Mach. Summ. Curr. Res., Springer International Publishing, Cham, 2019: pp. 1–71. https://doi.org/10.1007/978-3-030-16800-1_1.

[92] B. Veeraraghavan, A. Durairajan, B. Haran, B. Popov, R. Guidotti, Study of Sn-Coated Graphite as Anode Material for Secondary Lithium-Ion Batteries, J. Electrochem. Soc. 149 (2002) A675. https://doi.org/10.1149/1.1470653.

[93] Z.-S. Wu, W. Ren, L. Xu, F. Li, H.-M. Cheng, Doped Graphene Sheets As Anode Materials with Superhigh Rate and Large Capacity for Lithium Ion Batteries, ACS Nano. (2011) 5463–5471.

[94] J. Yang, M. Xu, J. Wang, S. Jin, B. Tan, A Facile Approach to Prepare Multiple Heteroatom-Doped Carbon Materials from Imine-Linked Porous Organic Polymers, Sci. Rep. 8 (2018) 1–11. https://doi.org/10.1038/s41598-018-22507-2.

[95] T. Pillar-Little, D.Y. Kim, Differentiating the impact of nitrogen chemical states on optical properties of nitrogen-doped graphene quantum dots, RSC Adv. 7 (2017) 48263–48267. https://doi.org/10.1039/c7ra09252k.

[96] F.A. Permatasari, A.H. Aimon, F. Iskandar, T. Ogi, K. Okuyama, Role of C-N Configurations in the Photoluminescence of Graphene Quantum Dots Synthesized by a Hydrothermal Route, Sci. Rep. 6 (2016) 1–8. https://doi.org/10.1038/srep21042.

[97] W. Wu, J. Shi, Y. Liang, F. Liu, Y. Peng, H. Yang, A low-cost and advanced SiOx-C composite with hierarchical structure as an anode material for lithium-ion batteries, Phys. Chem. Chem. Phys. 17 (2015) 13451–13456. https://doi.org/10.1039/c5cp01212k.

[98] A. Díaz-Álvarez, V. Cadierno, Glycerol: A promising Green Solvent and Reducing Agent for Metal-Catalyzed Transfer Hydrogenation Reactions and Nanoparticles Formation, Appl. Sci. 3 (2013) 55–69. https://doi.org/10.3390/app3010055.

[99] S. Komaba, K. Shimomura, N. Yabuuchi, T. Ozeki, H. Yui, K. Konno, Study on polymer binders for high-capacity SiO negative electrode of Li-Ion batteries, J. Phys. Chem. C. 115 (2011) 13487–13495. https://doi.org/10.1021/jp201691g.

[100] S. Komaba, N. Yabuuchi, T. Ozeki, K. Okushi, H. Yui, K. Konno, Y. Katayama, T. Miura, Functional binders for reversible lithium intercalation into graphite in propylene carbonate and ionic liquid media, J. Power Sources. 195 (2010) 6069–6074. https://doi.org/10.1016/j.jpowsour.2009.12.058.

[101] B.D. Assresahegn, D. Bélanger, Effects of the Formulations of Silicon-Based Composite Anodes on their Mechanical, Storage, and Electrochemical Properties, ChemSusChem. 10 (2017) 4080–4089. https://doi.org/10.1002/cssc.201701281.

[102] G. Xia, C. Wang, P. Jiang, J. Lu, J. Diao, Q. Chen, Nitrogen/oxygen co-doped mesoporous carbon octahedrons for high-performance potassium-ion batteries, J. Mater. Chem. A. 7 (2019) 12317–12324. https://doi.org/10.1039/c8ta12504j.